Cement & Concrete Composites 34 (2012) 1053–1060

Contents lists available at SciVerse ScienceDirect

Cement & Concrete Composites

journal homepage: www.elsevier.com/locate/cemconcomp

Analysis of pore structure, contact angle and pore entrapment of blended cement pastes from mercury porosimetry data

Qiang Zeng [a,b], Kefei Li [a,*], Teddy Fen-Chong [b], Patrick Dangla [b]

[a] Civil Engineering Department, Tsinghua University, 100084 Beijing, China
[b] Université Paris-Est, Laboratoire Navier ENPC-IFSTTAR-CNRS, 2 allée Kepler, 77420 Champs-sur-Marne, France

ARTICLE INFO

Article history:
Received 3 March 2011
Received in revised form 22 February 2012
Accepted 9 June 2012
Available online 16 June 2012

Keywords:
Mercury intrusion porosimetry
Fly-ash
Contact angle
Pore entrapment
Pore structure
Tortuosity

ABSTRACT

The mercury intrusion porosimetry (MIP) was used to investigate the pore structure characteristics of fly-ash cement pastes with two water to binder ratios (w/b = 0.3, 0.5). The total porosity, pore fraction distribution, contact angle hysteresis and the pore entrapment are quantified from the intrusion/extrusion data. The tortuosity of pore structure is further calculated from pore entrapment. The results show: (1) the w/b ratio is determinant for the formation of pore structure patterns, high w/b ratio providing high porosity, high connectivity but low pore surface roughness to pore structure; (2) the contact angle hysteresis can be related to pore surface roughness, the hysteresis factor α_θ attaining respectively 0.42, 0.75 for Paste I (w/b = 0.5) and Paste II (w/b = 0.3) samples at 180 d; (3) the tortuosity and the porosity obey just roughly the power law and more pore characteristics are needed to describe the tortuosity of blended cement pastes.

1. Introduction

Portland cement blended with mineral admixtures such as fly-ash is widely used in the production of cementitious materials for both performance and ecological considerations. These cementitious materials, after hydration and hardening, are typical heterogeneous porous media, and their mechanical and transport properties are intimately related to the pore structure [1]. Compared to the hydration process and mechanical properties, the pore structure is less understood for cement-based materials blended with fly-ash. The mercury intrusion porosimetry (MIP) is a commonly used method for characterizing the pore size distribution of porous materials [2–4]. Its principle lies in the fact that the intrusion volume of mercury depends on the applied external pressure to overcome the surface tension of mercury in pores. Thus the mercury intrusion (extrusion) process can be quantified by intrusion (extrusion) volume versus increasing (decreasing) pressure. If the pore geometry is idealized as cylindrical, the pore diameter (size) d can be related to the applied pressure P through Washburn equation [5],

$$d = -\frac{4\gamma\cos\theta}{P} \tag{1}$$

where γ is the surface tension of mercury (0.485 N/m) and θ is the contact angle between mercury and pore wall. Through this relation the pore size in terms of intrusion volume can also be determined.

Different volume–pressure (pore size) paths are usually obtained for the intrusion and extrusion processes for cement-based materials, named as the mercury hysteresis [6,7]. Two mechanisms are responsible for this phenomenon. The first is the contact angle hysteresis, i.e. the contact angle between mercury and pore wall adopts different values, $\theta_{in,ex}$, for intrusion and extrusion, see Fig. 1. Through a corrugated pore structure model (CPSM), Salmas and Androutsopoulus [8] deduced $\theta_{in} = 143^\circ$ and $\theta_{ex} = 100.5^\circ \sim 128^\circ$ for different porous materials with controlled pore structure. Shi and Winslow [9] found a nearly constant advancing contact angle, $\theta_{in} \approx 130^\circ$, for blended cement pastes. For cement pastes and mortars, the receding angle was measured as $\theta_{ex} = 104^\circ$ through single intrusion–extrusion cycle [10] and multiple cycles [11–13]. Second mechanism for mercury hysteresis is the connectivity of pore structure. Due to the "ink-bottle" shape pores the size from Eq. (1) is actually the size of "pore neck" that connects larger pores. Thus, Diamond [14] concluded that MIP could only provide threshold diameters of pores in the intrudable porosity. However, other authors state that acceptable estimation of pore structure can be obtained from MIP data through strict experimental control and proper interpretation [11,13,15,16]. Fig. 2 illustrates the mechanisms using MIP data in this paper.

Thus, mercury hysteresis contains pertinent information on physical properties of pore wall as well as the connectivity of pore structure. However, deepened analysis of mercury hysteresis is rare even with large volume of MIP data published in literature so far. This paper attempts to analyze the two mechanisms quantitatively from MIP data and relate the hysteresis to the pore

* Corresponding author. Tel./fax:+86 10 6278 1408.
E-mail address: likefei@tsinghua.edu.cn (K. Li).

0958-9465/$ - see front matter © 2012 Elsevier Ltd. All rights reserved.
http://dx.doi.org/10.1016/j.cemconcomp.2012.06.005

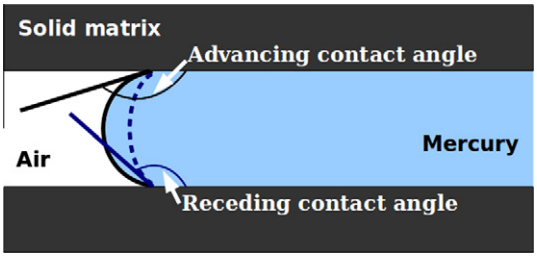

Fig. 1. Schematic illustration of the mercury advancing and receding contact angles.

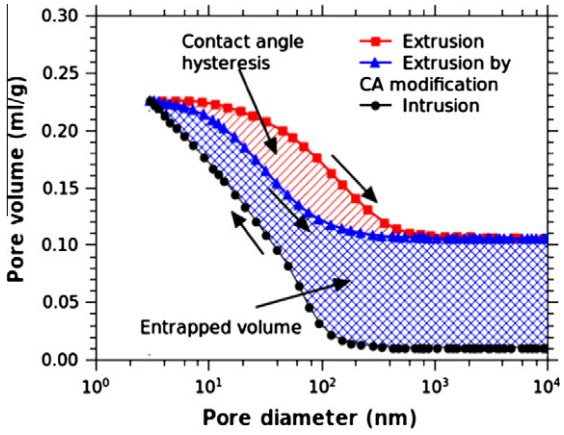

Fig. 2. Illustration of mercury hysteresis in MIP intrusion/extrusion and its mechanisms (Line-shaded area for contact angle hysteresis, grid-shaded area for pore connectivity, "CA" for contact angle).

properties and structure evolution for blended cement pastes. To this aim, cement pastes incorporating different fly-ash contents are prepared. The pore structure and its evolution are investigated by MIP method. From the intrusion data, the total porosity is evaluated for all samples and the pore size fraction is estimated with the advancing contact angle retained as 130°. From the extrusion data, the contact angle hysteresis is quantified through a hysteresis factor, and the pore entrapment due to "ink-bottle" effect (connectivity) is obtained through the contact angle correction. Furthermore, the paper investigates the impact of w/b ratio, fly-ash content and curing age on the contact angle hysteresis and pore entrapment. Finally, the tortuosity of pore structure is evaluated on the basis of the pore entrapment measurement.

2. Materials and experiment

A Type I Portland cement and a low calcium fly-ash are used in the study, and the chemical composition and physical properties of cement and fly-ash are presented in Table 1. The mineral contents of cement were evaluated from Bogue's procedure [17] as: C_2S (21.38%), C_3S (58.88%), C_3A (6.49%), C_4AF (8.77%), Gypsum (0.75%) and others (3.73%). Blended cement paste samples were prepared with two water to binder (w/b) ratios (0.3, 0.5), and four fly-ash contents, see Table 2 for detailed proportioning. The fly-ash content is defined as the mass ratio between fly-ash and total binder (fly-ash and cement). After mixing, cement pastes were cast into cylinder tubes of 10 mm diameter and placed in room condition with temperature controlled at 20 °C. The specimens were demoulded from the tubes at the age of 3 d and kept in water. To avoid the possible leaching, the ratio of specimen to water was kept at roughly 1:1 in volume or 2:1 in weight. At given curing ages (7 d, 28 d, 90 d and 180 d), the samples were ground to particles with

Table 1
Chemical composition and physical properties of cement and fly-ash.

Chemical composition/physical properties	Cement	Fly-ash
Silica (SiO_2, %)	22.93	57.60
Alumina (Al_2O_3, %)	4.29	21.90
Iron oxide (Fe_2O_3, %)	2.89	2.70
Calcium oxide (CaO, %)	66.23	7.80
Magnesium oxide (MgO, %)	1.92	1.68
Sulfur trioxide (SO3, %)	0.35	0.41
Sodium oxide (Na_2O(eq), %)	0.70	1.05
Free calcium oxide (CaO(f), %)	0.64	–
Chloride (Cl, %)	0.006	–
Loss on ignition (LOI, %)	1.70	7.05
Density (g/ml)	3.12	2.06
Specific area (m^2/kg)	343	355

size of 1–2 mm. This sample size was reported capable to avoid additional pore volume entrapment by the size effect during MIP operation [10]. The freezing-drying method is used instead of traditional oven-drying to minimize the possible induced drying damage to samples. The samples, together with the container, were firstly immersed into liquid nitrogen (N_2, −196 °C) for 5 min, then transferred to the freeze-dryer and vacuumed for 48 h. The outgass pressure was controlled to be less than 15 Pa. The freezing-dried samples of blended cement pastes were then tested for pore distribution by MIP (Autopore IV 9510, Tsinghua University) with the applied maximum and minimum pressures controlled to 414 MPa and 1.4 kPa. The equilibrium time for each applied pressure level was controlled to 10 s. And the maximum and minimum applied pressures correspond to cylindrical pore sizes of 3 nm and 800 μm respectively.

3. Intrusion phase: pore volume and pore size fraction

3.1. Intruded pore volume

The intruded mercury volumes were recorded and converted to porosity, presented in Fig. 3 for different curing ages. Generally, with curing age the hydration of cement advances, solid hydration products form and the microstructure becomes denser. As fly-ash is blended into cement, its hydration is much slower and can fill the already-formed pores by its own hydrates. Thus, the pore volume is determined by w/b ratio, curing age as well as the fly-ash content [18,19]. However, from Fig. 3 it is obvious that the w/b is predominant factor for pore volume and Paste I samples have larger pore volume than Paste II samples for all cases. That is because the w/b ratio determines both the hydration degree of cement (and fly-ash) and the physical packing patterns of formed solid hydration products [18]. As for curing age, the total porosity, in Fig. 3, decreases with the curing age due to the continuous hydration of cement grains and the pozzolanic reaction of fly-ash particles.

In the figure, the porosity increases with the fly-ash content, surely due to the "dilution" effect of the less reactive fly-ash [20,21]. But, it is also noted that this porosity increase can be reduced to a negligible level as w/b is low, fly-ash content is less than 60% and curing age is long, see porosity of PII0 (0%FA), PII1 (20%FA) and PII2 (40%FA) samples in Fig. 3. In fact, the above is exactly the principle of industrial application of fly-ash as secondary cementitious material (SCM) in cements [18].

3.2. Pore size fraction

The relation in Eq. (1) should be used to obtain the pore volume-size relation from the measured volume–pressure relation in intrusion phase. The advancing contact angle θ_{in} is not measured separately for Paste I and II samples. From the aforementioned

Table 2
Composition of blended cement pastes (for 1 l).

Paste	w/b	Sample	Cement (g)	Fly-ash (g)	Water (g)	Fly-ash content (%)
I	0.5	PI0	1218	0	609	0
		PIF1	957	234	596	20
		PIF2	677	451	559	40
		PIF3	435	650	543	60
II	0.3	PII0	1612	0	484	0
		PIIF1	1224	306	459	20
		PIIF2	874	583	437	40
		PIIF3	556	834	417	60

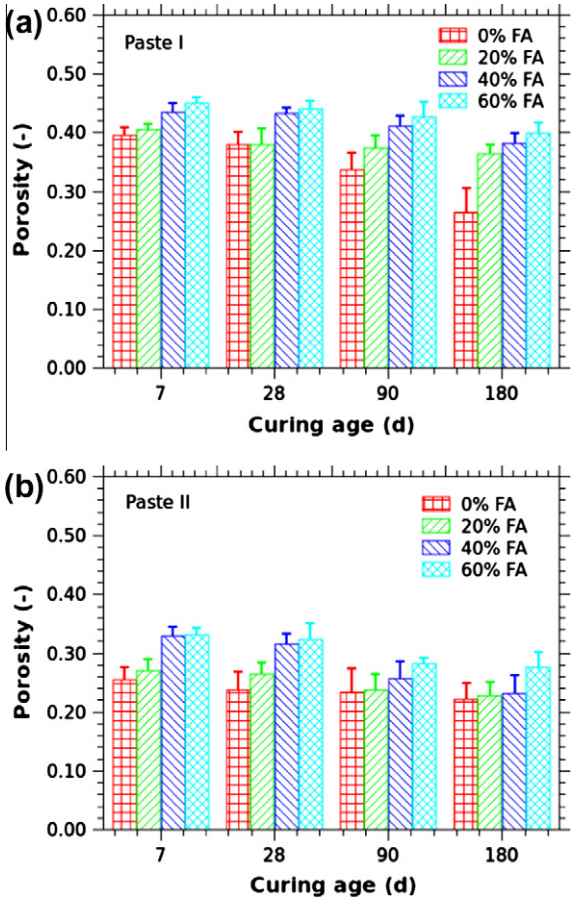

Fig. 3. Pore volume of Paste I (a) and Paste II (b) samples at different curing age.

literature results the advancing contact angle seems to be rather stable, θ_{in} being around 130°. Thus, as an application, the pore size fraction is evaluated for all samples with assumption $\theta_{in} = 130°$ and the intruded pore volume fraction in terms of pore size (diameter) is illustrated here.

In Fig. 4, the pore size fractions (PSF) of Paste I samples collapse nearly into one curve with curing age. That means, irrespective of the absolute intrusion volume, the composition of pore structure from different pore ranges remains the same. A closer observation on top half of Fig. 4 reveals that the PSF curve of neat sample PI0 (Paste I) at 180 d lies above the others for pore size range of $d > 100$ nm, meaning that the neat paste sample contains more coarser pores. This is actually an evidence of pore refinement effect of fly-ash through both physical filling and pozzolanic reaction. On the contrary, the PSF shows larger divergence for Paste II samples with curing age. Under $w/b = 0.3$, the samples achieve a more compact structure and the filling effect of FA particles is not as important as for Paste I samples. Thus the pore refinement of fly-ash comes mainly from its own hydration process. At 180 d, the higher the fly-ash content the more the samples contain smaller pores. Again, this observation is in relative sense and the porosity fraction for a given pore size should be determined together with the porosity presented in Section 3.1.

Fig. 5 illustrates the PSF of all samples in terms of curing age. A first observation is that pore size becomes finer (smaller) with increasing curing age. However, significant difference is observed for the PSF evolution patterns for Paste I and II samples. As showed in Fig. 5, the PSF for Paste I samples seems to stabilize for curing age of 180 d compared to the PSF at 90 d, regardless of the fly-ash content. That indicates, under a high water availability, both cement grains and fly-ash particles undergo a relatively advanced degree of hydration and the hydrates formation stabilizes at 180 d. However, very important difference is observed between PSFs at 90 d and 180 d for Paste II samples, showed in the bottom half of Fig. 5. That implies the secondary hydration, from fly-ash particles, continues contributing to the pore filling process by its own hydration product. It seems that this process is not yet in its stabilized phase at 180 d. At age of 180 d, the pore size distribution contains 60–90% pores with $d < 10$ nm and 10–40% pores larger than this value. The more the fly-ash content, the more this distribution approaches binary: with 90% smaller than 10 nm and 10% larger than 10 nm for fly-ash content of 60%. And this value of pore size is coined as the threshold pore size for cement-based porous materials [2].

4. Extrusion phase: contact angle and pore entrapment

4.1. Contact angle

From surface physics the contact angle hysteresis belongs to the intrinsic properties of the contact interface between pore wall and liquids [22]. Here a factor, α_θ, is defined to quantify the contact angle hysteresis:

$$\alpha_\theta = \frac{\cos\theta_{in} - \cos\theta_{ex}}{\cos\theta_{in}} = 1 - \frac{\cos\theta_{ex}}{\cos\theta_{in}} \tag{2}$$

The hysteresis factor α_θ scales in fact the importance of contact angle hysteresis. Note that the contact angles between pore wall and mercury are obtuse ($\theta_{in,ex} > 90°$) and usually the extrusion angle θ_{ex} is inferior to the intrusion angle θ_{in}. Therefore the hysteresis factor α_θ is a monotonous function of contact angle hysteresis: the bigger is the difference between $\theta_{in,ex}$ the larger α_θ is. During the MIP test, as the intrusion phase reaches its end the applied pressure attains its maximum value P_{max}. As the extrusion phase begins, the applied pressure drops but the mercury volume does not change instantaneously, i.e. the mercury begins to flow out only at a certain pressure drop ΔP. If this pressure drop is only attributed to the contact angle hysteresis, the factor α_θ can be evaluated through Eqs. (1) and (2) as,

$$-\frac{4\gamma\cos\theta_{in}}{P_{max}} = -\frac{4\gamma\cos\theta_{ex}}{P_{max} - \Delta P}, \quad \alpha_\theta = \frac{\Delta P}{P_{max}} \tag{3}$$

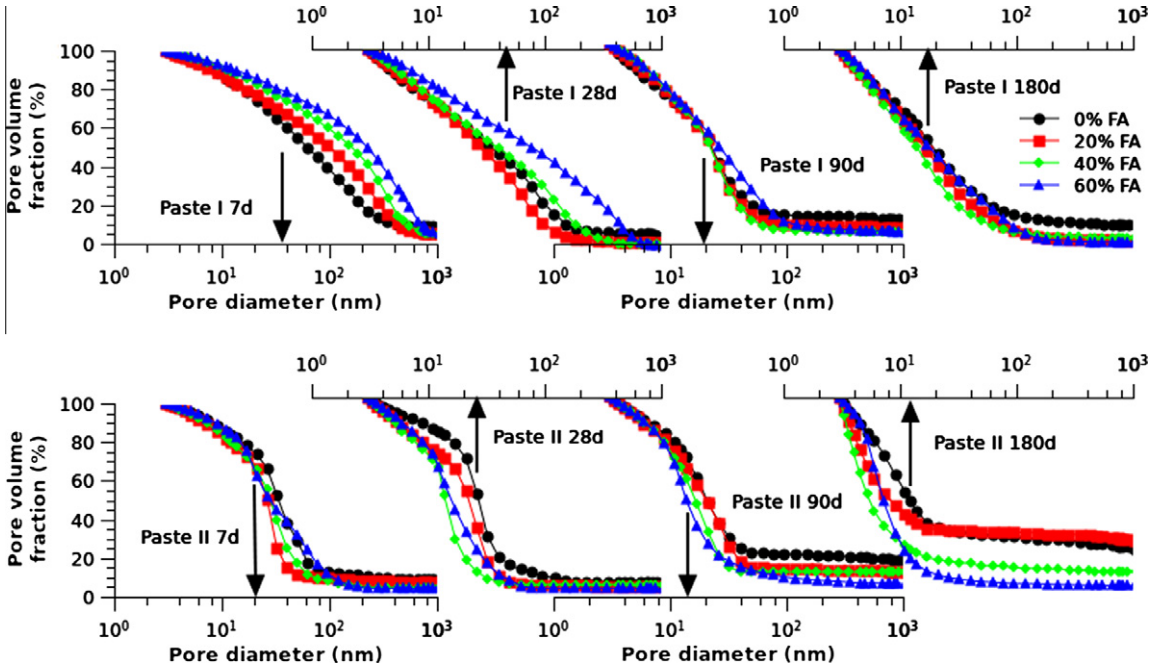

Fig. 4. Intrusion volume fractions for Paste I (up) and Paste II (down) samples with different fly-ash contents.

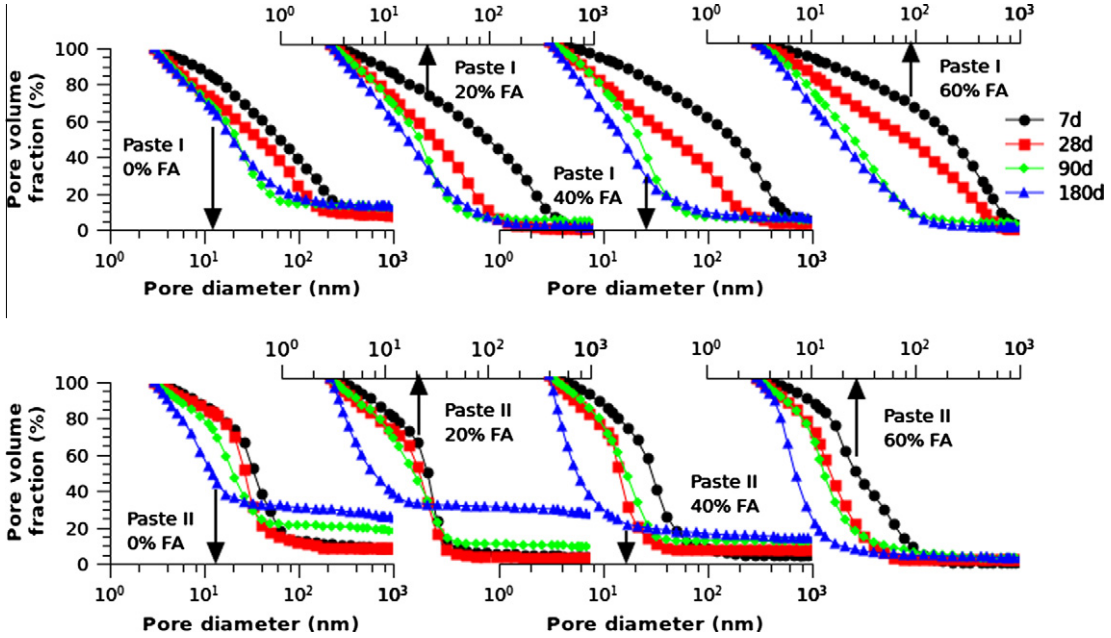

Fig. 5. Intrusion volume fractions for Paste I (up) and Paste II (down) samples at different curing ages.

The hysteresis factor for a specific intrusion–extrusion cycle can be determined through the above equation with the maximum applied pressure and the corresponding pressure drop. Although the maximum pressure corresponds to the smallest pores, the extrusion process can involve also bigger pores as the "ink-bottle" geometry is considered for pore structure. Here, the hysteresis factor by contact angle shift is considered as an overall property for the whole pore range.

The hysteresis factors for all samples in terms of fly-ash content are presented in Fig. 6. It is observed that the impact of fly-ash content on the contact angle hysteresis is different for Paste I and Paste II samples. For Paste I samples the hysteresis factor α_θ increases with the fly-ash content while the factor is rather constant for Paste II samples, $\alpha_\theta \approx 0.8$, regardless of the fly-ash content. This is related to the pore structure formation process of pastes under different w/b ratios. For Paste I samples ($w/b = 0.5$) the water supply is sufficient for the hydration of both cement grains and fly-ash particles. Physically, the fly-ash particles "dilute" the cement grains and act as nucleation sites for precipitation of cement hydration products [21]. Thus, fly-ash contributes to the hydration extent of cement, and the hydrates precipitating in pores can augment the roughness of pore surface (wall). This augmentation of pore roughness can explain the increase of contact angle hysteresis with fly-ash content [23,24]. However, for Paste II

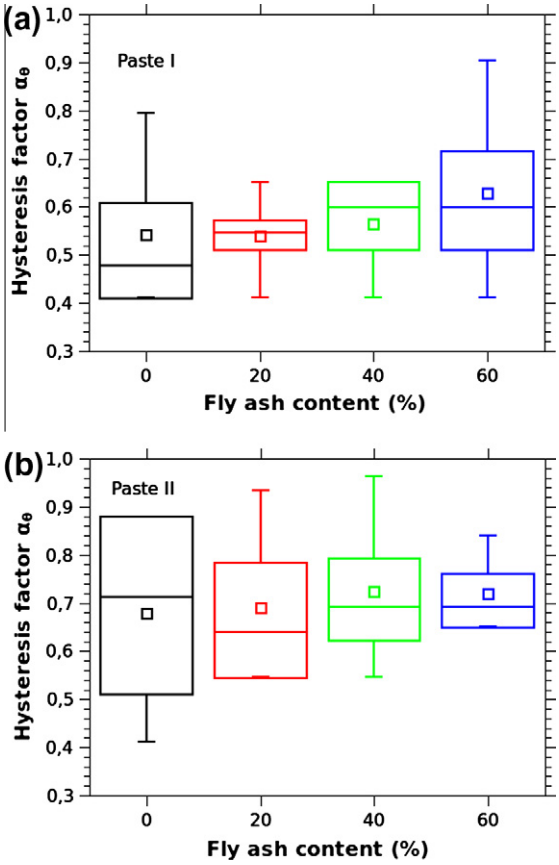

Fig. 6. Hysteresis factor of contact angle α_θ for Paste I (a) and Paste II (b) samples with different fly-ash contents (□: mean value, ⊟: middle 50% limit, I: value range).

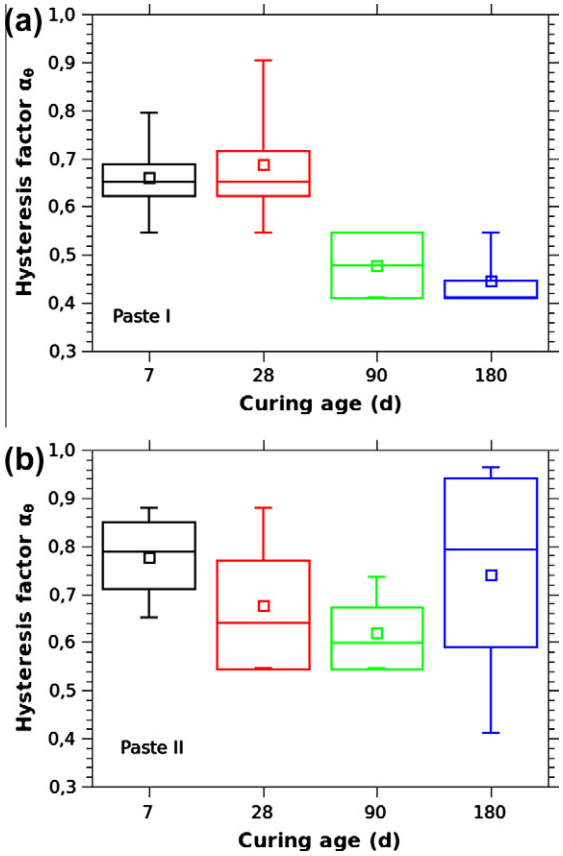

Fig. 7. Hysteresis factor of contact angle α_θ for Paste I (a) and Paste II (b) samples at different curing ages (□: mean value, ⊟: middle 50% limit, I: value range).

samples ($w/b = 0.3$) the water is not sufficient for cement hydration, a rather compact pore structure is formed since the beginning of hydration and the hydration extent is much limited by water availability regardless of the fly-ash content. Accordingly, less difference is found for pore surface roughness for Paste II samples [25], explaining the nearly constant hysteresis factor for all Paste II samples.

The hysteresis factors for all samples in terms of curing age are presented in Fig. 7. It appears that the hysteresis factor α_θ decreases with curing age for Paste I and Paste II samples. That means the contact angle hysteresis becomes less important with curing age. The roughness analysis of pore surface for the same samples, provided by Zeng et al. [25], showed that with the curing age the hydration process of fly-ash particles, pozzolanic reaction, consumes the pore hydrates from cement grains and tends to "flatten" the pore surface. This mechanism can also explain the decrease of contact angle hysteresis with curing age. Similar results were also obtained by Zhou et al. [26] on cement pastes of $w/b = 0.4$.

4.2. Pore entrapment

The pore entrapment can be evaluated directly from the difference between intrusion curve and extrusion curve for the same applied pressure,

$$\mathcal{V}_{\text{en}}^{P}(P_{\text{in}} = P_{\text{ex}} = P_i) = (\mathcal{V}_{\text{in}} - \mathcal{V}_{\text{ex}})|_{P_{\text{in}}=P_{\text{ex}}=P_i} \tag{4}$$

However this entrapment cannot be related directly to a specific pore size d since different contact angles $\theta_{\text{ex,in}}$ in Washburn's equation link same P_i to two different pore sizes $d_{\text{ex,in}}$. For a same pore size d, the intrusion pressure and extrusion pressure can be expressed as,

$$P_{\text{in}} = -\frac{4\gamma\cos\theta_{\text{in}}}{d}, \quad P_{\text{ex}} = -\frac{4\gamma\cos\theta_{\text{ex}}}{d} = -\frac{4\gamma\cos\theta_{\text{in}}}{(1-\alpha_\theta)d} \tag{5}$$

where α_θ is the hysteresis factor of contact angle. Thus, the intrusion curve and extrusion curve can all be expressed in terms of one unique variable, $d/\cos\theta_{\text{in}}$, and the pore entrapment volume can be expressed as,

$$\mathcal{V}_{\text{en}}\left(\frac{d_i}{\cos\theta_{\text{in}}}\right) = \mathcal{V}_{\text{in}}\left(\frac{d}{\cos\theta_{\text{in}}}\right) - \mathcal{V}_{\text{ex}}\left(\frac{d}{\cos\theta_{\text{in}}}\right)|_{d=d_i} \tag{6}$$

To facilitate the discussion, the pore entrapped volume is noted in terms of its fraction instead of absolute value. The pore entrapment fraction, α_{en}, for a specific pore size d is defined as the ratio between the pore entrapment volume and the total intrusion volume,

$$\alpha_{\text{en}}\left(\frac{d}{\cos\theta_{\text{in}}}\right) = \mathcal{V}_{\text{en}}\left(\frac{d}{\cos\theta_{\text{in}}}\right)/\mathcal{V}_{\text{in}}^{\text{total}} \tag{7}$$

Not losing the generality, we assume a specific value for intrusion contact angle, $\theta_{\text{ex}} = 130^\circ$, so that the pore entrapment fraction α_{en} can be linked directly to the pore size d. The distribution of entrapped pore fraction α_{en} is illustrated in Fig. 8 in terms of pore size. Firstly at 180 d, Paste II samples have higher entrapment fraction than Paste I samples, meaning the pore structure of the former is more complicate. For Paste I samples, the distribution curves tend to collapse into one curve with curing age. At 180 d the characteristic pore sizes of entrapment, corresponding to the maximum of

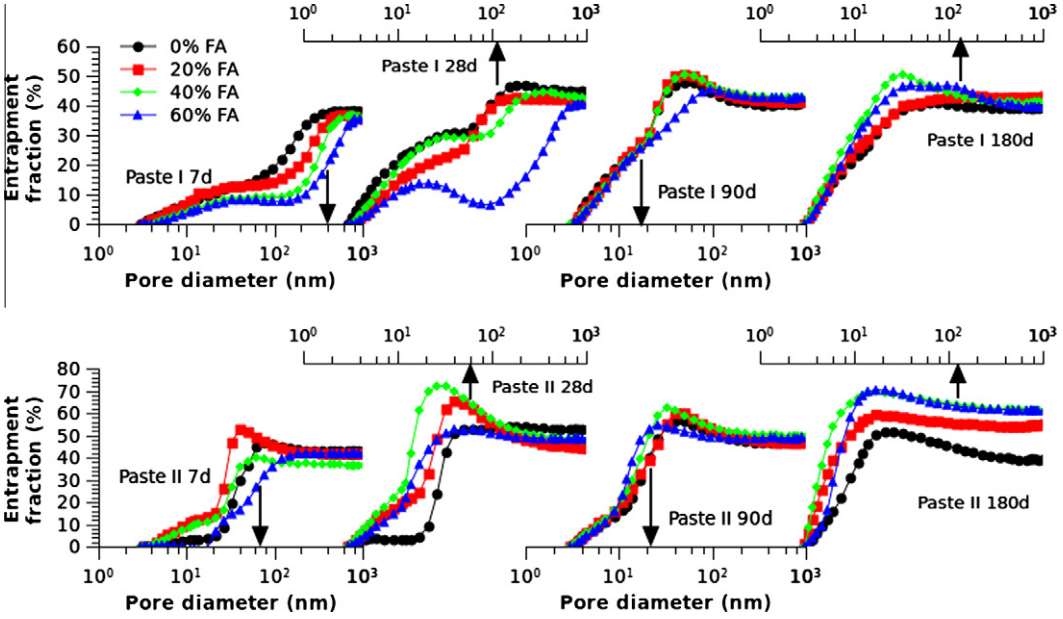

Fig. 8. Entrapped volume fraction for Paste I (up) and II (down) samples at different age.

pore entrapment, are rather different for different samples and fly-ash content tends to increase this pore size. On the contrary, the distribution curves tend to diverge among the Paste II samples but the characteristic pore sizes of entrapment are nearly the same for all Paste II samples.

The total fraction of pore entrapment is plotted in terms of fly-ash content in Fig. 9. One can see that the fly-ash content has not notable impact on the total entrapment fractions, neither for Paste I samples nor for Paste II samples. On the contrary, as illustrated in Fig. 10, substantial increase is observed for the pore

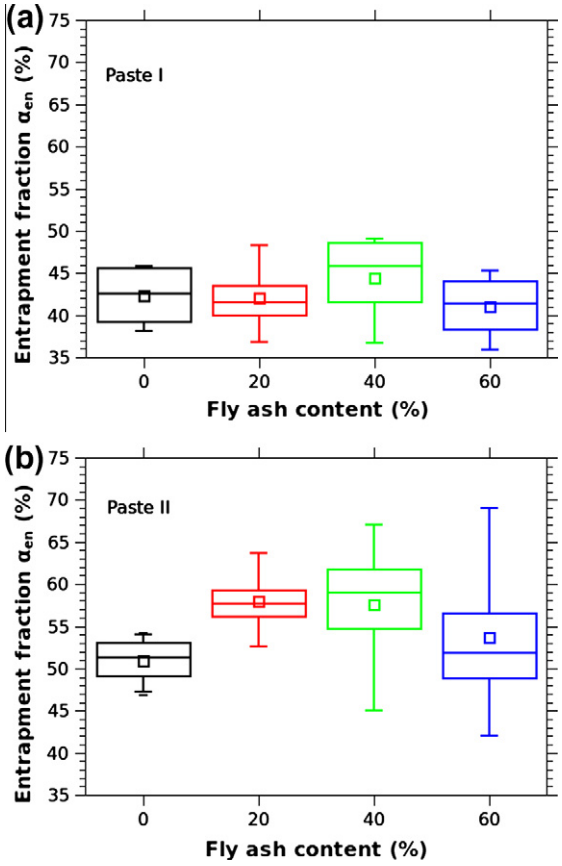

Fig. 9. Total fraction of pore entrapment for Paste I (a) and Paste II (b) samples with different fly-ash content (□: mean value, ⊟: middle 50% limit, I: value range).

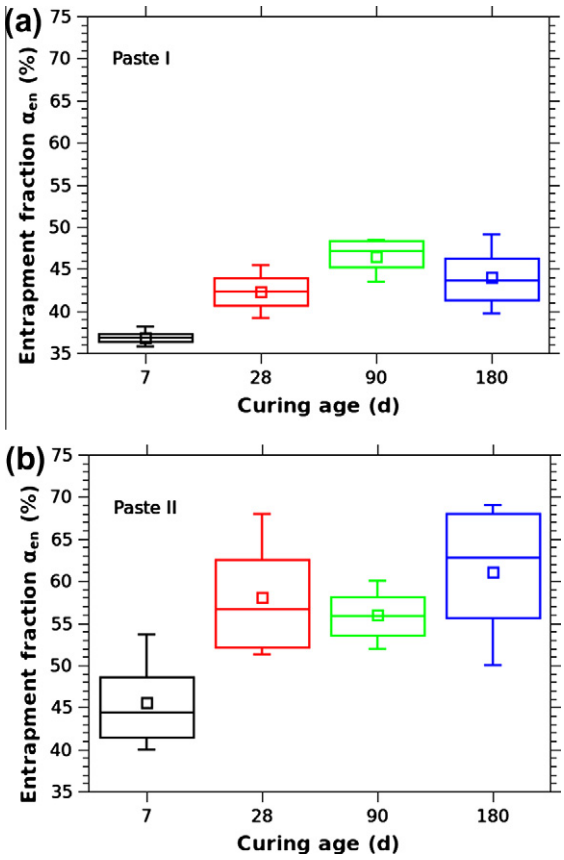

Fig. 10. Total fraction of pore entrapment for Paste I (a) and Paste II (b) samples with different curing age (□: mean value, ⊟: middle 50% limit, I: value range).

entrapment fraction with curing age, from 36% to 42% (Paste I) and from 40% to 52% (Paste II), as curing age changes from 7 d to 180 d. This observation reflects, in fact, the pore refinement process by fly-ash hydration, generating more and more isolated pores in pore structure for Paste I and II samples.

5. Discussion

For all samples (Paste I and Paste II), an important extent of pore entrapment has been observed, approaching 50% of total porosity. Thus, the pore size distribution evaluated directly from Washburn equation can only be regarded as the "neck" size that percolates bigger pores. Under this image, the pore entrapment can provide useful information to describe the complexity of pore structure. One application is to deduce the tortuosity of pore structure from the pore entrapment measurement.

The tortuosity of pore structure, τ, is defined as the distance of continuous path between two points in pore structure divided by their straight line length [27]. This value reflects actually the degree of difficulty of mass transport in the (connected) pore structure. Thus, it is a fundamental property for mass transfer through both diffusion and permeation processes [28]. In the literature, several models are proposed to express the tortuosity in terms of the pore entrapment fraction α_{en} or in terms of (partial) porosity [8,29,30]. Salmas and Androutsopoulos [30] obtained a relationship between tortuosity and pore entrapped volume fraction through CPSM model,

$$\tau = 4.6242 \ln\left(\frac{4.996}{1-\alpha_{en}} - 1\right) - 5.8032 \tag{8}$$

The tortuosity values for all samples are illustrated in Fig. 11 and it can be observed that the tortuosity of Paste II samples is systematically higher than Paste I samples. This observation is consistent with the pore entrapment results in Fig. 8, indicating Paste II samples adopt more complex pore structure.

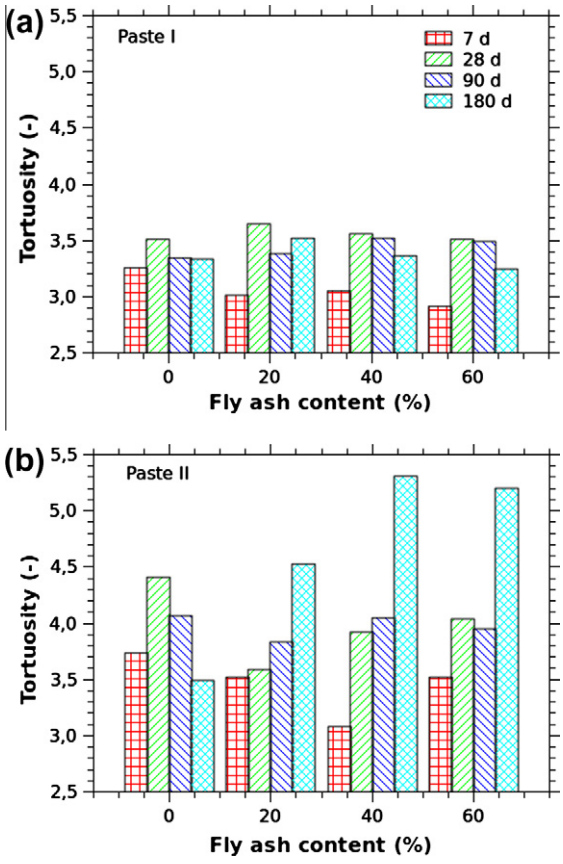

Fig. 11. Tortuosity values for Paste I (a) and Paste II (b) by CPSM model [30].

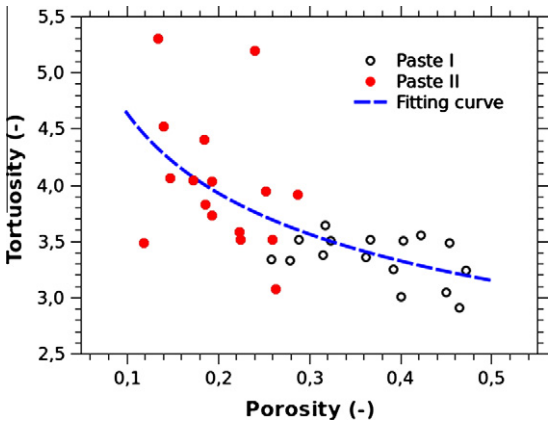

Fig. 12. Tortuosity for Paste I and II samples in terms of porosity regressed by Archie's law ($a = 0.3753$, $m = 1.2414$).

The tortuosity of porous media can also be evaluated from electrical conductivity measurement. By definition the tortuosity τ is expressed in terms of the material conductivity σ_t, the pore solution conductivity σ_l and the porosity ϕ as, $\tau = \phi\sigma_l/\sigma_t$. Archie' law [31] expresses the conductivity ratio σ_t/σ_l in terms of porosity through a power relation,

$$\frac{\sigma_t}{\sigma_l} = a\phi^m \tag{9}$$

with a, m as two Archie coefficients. By the above two relations the tortuosity can be evaluated as,

$$\tau = a^{-1}\phi^{1-m} \tag{10}$$

Fig. 12 presents the tortuosity values for all samples, in terms of total porosity, through the above equation with the Archie's coefficients regressed as $a = 0.3753$, $m = 1.2414$. It can be seen that the tortuosity and the porosity obey roughly the Archie's law but with a relatively large dispersion, especially for Paste II samples. It is in fact related to the rougher surface and poorer connectivity of pores generated by low w/c in blended cement pastes. Accordingly, detailed descriptions on surface roughness and connectivity geometry will be necessary to ameliorate precision of the power law in Eq. (10).

6. Concluding remarks

1. From the MIP data in intrusion phase, it is clear that the w/b ratio, compared to fly-ash content and curing age, is predominant factor for both total porosity and pore size distribution. For Paste I samples ($w/b = 0.5$), high water availability induces coarser pore structure, the filling effect of products from fly-ash secondary hydration is notable and the pore size range distribution for all Paste I samples is rather identical. For Paste II sample ($w/b = 0.3$), the low water content limits greatly both hydrations of cement and fly-ash. A dense pore structure is formed from very beginning of material setting, thus the filling effect of fly-ash hydration is less important. And the pore range distribution is much influenced by fly-ash content.
2. From MIP data in extrusion phase, the contact angle hysteresis is characterized by a hysteresis factor α_θ, determined by the pressure drop at the beginning of extrusion phase. This hysteresis involves both intrinsic properties of pore surface (wall) and the pore geometry, e.g. "ink-bottle" pores. From our analysis, the hysteresis factor is consistent with the possible contribution

of secondary hydration of fly-ash to pore surface roughness. The increase of hysteresis factor with fly-ash content may be related to the contribution of fly-ash hydration products to pore surface roughness. And the decrease of hysteresis factor for a same sample with curing age may indicate the consumption of cement hydrates by fly-ash hydration tends to "flatten" the pore surface.

3. The pore entrapment, denoted by entrapment fraction α_{en}, reflects to what extent the pore structure derives from the geometry assumption of serial cylindric pores. The low connectivity of pores of Paste II samples gives higher entrapment fraction, around 70% for PIIF3 sample. That implies, for pastes blended with fly-ash, the serial cylindric tube model can greatly distort the real pore structure. The characteristic pore size for entrapment is well correlated to the threshold pore size from intrusion data and both sizes can characterize the smallest percolating pores.
4. On the basis of pore entrapment fraction, the tortuosity of pore structure is evaluated through a CPSM model and it is found that low connectivity of pores also induces larger tortuosity value, Paste II samples having systematical higher tortuosity than Paste I samples. The correlation analysis between the tortuosity and the porosity shows that the τ–ϕ relation just roughly obeys the power law and large dispersion is obtained especially for low connectivity pore structure (Paste II). For accurate prediction of tortuosity more pore structure characteristics, such as surface roughness and connectivity details, should be taken into account.

Acknowledgment

The study is supported by China National Major Fundamental Research Grant (973 Program, No. 2009CB623106).

References

[1] Jennings HM. Towards establishing relationships between microstructure and properties of cement based materials. Ceram Trans 1990;16:289–317.
[2] Winslow DN, Diamond S. A mercury porosimetry study of the evaluation of porosity in Portland cement. ASTM J mater 1970;5:564–85.
[3] Orr C. Application of mercury penetration to materials analysis. Powder Technol 1970;3:117–23.
[4] Wardlaw NC, Mckeller M. Mercury porosimetry and the interpretation of pore geometry in sedimentary rocks and artificial models. Powder Technol 1981;29:127–43.
[5] Washburn EW. Note on a method of determining the distribution of pore sizes in a porous material. Proc Nati Acad Sci USA 1921;7:115–6.
[6] Giesche H, Unger KK, Muller U, Esser U. Hysteresis in nitrogen sorption and mercury porosimetry on mesoporous model adsorpbents made of aggragate monodisperse silica spheres. Colloids Surf 1989;37:93–113.
[7] Giesche H. Mercury porosimetry: a general (practical) overview. Part Part Syst Charact 2006;23:9–19.
[8] Salmas CE, Androutsopoulos GP. Mercury porosimetry: contact angle hysteresis of materials with controlled pore structure. J Colloid Interface Sci 2001;239:178–89.
[9] Shi D, Winslow DN. Contact angle and damage during mercury intrusion into cement paste. Cem Concr Res 1985;15:645–54.
[10] Moro F, Boehni H. Ink-Bottle effect in mercury intrusion porosimetry of cement-based materials. J Colloid Interface Sci 2002;246:135–49.
[11] Kaufmann JP, Loser R, Leemann A. Analysis of cement-based materials by multi-cycle mercury intrusion and nitrogen sorption. J Colloid Interface Sci 2009;336:730–7.
[12] Kaufmann JP. Characterization of pore space of cement-based materials by combined mercury and wood's metal intrusion. J Am Ceram Soc 2009;92:209–16.
[13] Kaufmann JP. Pore space analysis of cement-based materials by combined Nitrogen sorption – wood's metal impregnation and multi-cycle mercury intrusion. Cem Concr Compos 2010;32:514–22.
[14] Diamond S. Mercury porosimetry: an inappropriate method for the measurement of pore size distributions in cement-based materials. Cem Concr Res 2000;30:1517–25.
[15] Leóny León CA. New perspectives in mercury porosimetry. Adv Colloid interface Sci 1998;76–77:341–72.
[16] Rigby SP, Edler KJ. The Influence of mercury contact angle surface tension and retraction mechanism on the interpretation of mercury porosimetry data. J Colloid Interface Sci 2002;250:175–90.
[17] Bogue RH. Calculation of the compounds in Portland cement. Ind Eng Chem 1929;1:192–7.
[18] Metha PK, Monteiro PJM. Concrete: microstructure, properties and materials. Third ed. London: McGraw Hill; 2006.
[19] Cook RA, Hover KC. Mercury porosimetry of hardened cement pastes. Cem Concr Res 1999;29:933–43.
[20] Feldman RF, Carrate GG, Malhotra VM. Study on development of physical and mechanical properties of high volume fly-ash cement pastes. Cem Concr Comp 1990;12:245–51.
[21] Cyr M, Lawrence P, Ringot E. Mineral admixtures in mortars: quantification of the physical effects of inert materials on short-term hydration. Cem Concr Res 2005;35:719–30.
[22] Adamson AW, Gast AP. Physical chemistry of surface. 6th ed. New York: John Wiley & Sons; 1996.
[23] Grundke K, Bogumil T, Gietzelt T, Hacobasch HJ, Kwok DY, Newmann AW. Wetting measurement on smooth rough and porous solid surfaces. Progr Colloid Polym Sci 1996;101:56–68.
[24] Drelich J, Miller JD, Good RJ. The effect of drop (bubble) size on advancing and receding contact angles for heterogeneous and rough solid surfaces as observed with sessile-drop and captive-bubble techniques. J Colloid Interface Sci 1996;179:37–50.
[25] Zeng Q, Li K, Fen-Chong T, Dangla P. Surface fractal analysis of pore structure of high-volume fly-ash cement pastes. Appl Surf Sci 2010;257:762–8.
[26] Zhou J, Ye G, van Breugel K. Characterization of pore structure in cement-based materials using pressurization–depressurization cycling mercury intrusion porosimetry (PDC–MIP). Cem Concr Res 2010;40:1120–8.
[27] Vervoort RW, Cattle SR. Linking hydraulic conductivity and tortuosity parameters to pore space geometry and pore-size distribution. J Hydrol 2003;272:36–49.
[28] Bentz DP. Influence of silica fume on diffusivity in cement-based materials I Experimental and computer modeling studies on cement pastes. Cem Concr Res 2000;30:953–62.
[29] Androutsopoulos GP, Salmas CE. Tomography of macro–meso-pore structure based on mercury porosimetry hysteresis. Chem Eng Comm 2000;181:137–77.
[30] Salmas CE, Androutsopoulos GP. A novel pore structure tortuosity concept based on nitrogen sorption hysteresis data. Ind Eng Chem Res 2001;40:721–30.
[31] Archie GE. The electrical resistivity log as an aid to determining some reservoir characteristics. AIME Trans 1942;146:54–62.